Operando visualization of the hydrogen evolution reaction with atomic scale precision at different metal-graphene interfaces

Tomasz Kosmala,[a,c] Anu Baby,[b] Marco Lunardon,[a] Daniele Perilli,[b] Hongsheng Liu,[b] Christian Durante,[a] Cristiana Di Valentin,[b] Stefano Agnoli*[a] and Gaetano Granozzi[a]

a Dipartimento di Scienze Chimiche and INSTM Research Unit, Università degli Studi di Padova, Via Marzolo 1, 35131 Padova, Italy
b Dipartimento di Scienza Dei Materiali, Università Degli Studi di Milano-Bicocca, Via Roberto Cozzi 55, 20125, Milano, Italy
c Institute of Experimental Physics, University of Wrocław, pl. M. Borna 9, 50-204 Wrocław, Poland

The development of new catalytic materials for the hydrogen evolution reaction is of pivotal importance for the hydrogen economy. Here we show that thin Fe films covered by monolayer graphene exhibit an outstanding catalytic activity, surpassing even that of Pt. This was demonstrated exploiting a method based on the evaluation of the noise in the tunneling current of electrochemical scanning tunneling microscopy (EC-STM). In this way we mapped with atomic scale precision the electrochemical activity of the graphene/Fe interface, unraveling that single Fe atoms trapped within carbon vacancies and curved graphene areas on step edges are exceptionally active. Density functional theory (DFT) calculations confirmed the sequence of activity obtained in the experiments. This work exemplifies the potential of EC-STM as the only available technique to determine both the atomic structure and relative catalytic performance of atomically well-defined sites in electrochemical *operando* conditions and provides a detailed rationale for the design of novel catalysts based on a cheap and abundant metal like Fe.

1. Introduction

Catalysis with 2D materials is a fascinating topic that is gaining an ever-increasing momentum in the scientific community. Not only 2D materials have exceptional intrinsic activity in a large variety of reactions, but connected to the 2D nature of these systems, some special nanoscale phenomena may unfold, which lay the basis for radically new strategies to improve the chemical activity[1]. In this regard, the confined space between a 2D material and its support (Scheme 1a) represents an unconventional physicochemical environment that is accessible only by selected chemical species (e.g. hydrogen[2]), therefore having a strong impact on selectivity. In addition, reaction intermediates or activated transition state complexes can be subjected to supplementary interactions that can lead to significant changes in the reaction energy paths[3].

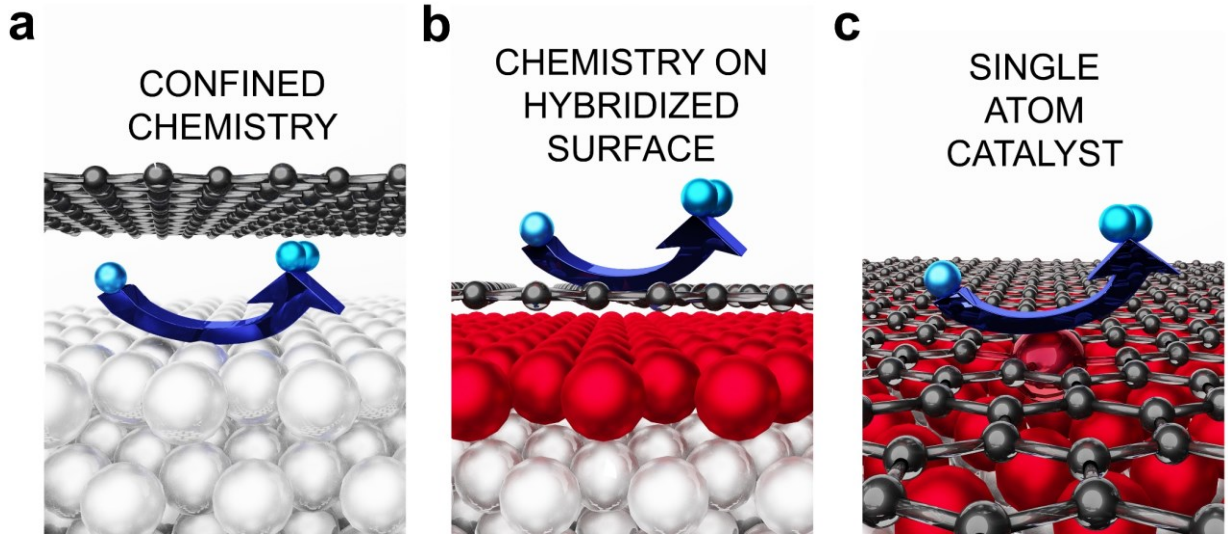

Figure 1. Interactions between a graphene layer and a metal substrate can lead to catalytic processes at different interfaces.

In this respect, a key aspect is the interfacial hybridization that can produce both electronic and structural changes, which can be exploited as a powerful tool to design novel functional materials (Scheme 1b). For example, it has been reported that the interfacial hybridization can induce enhanced chemical activity and improved stability even outside the electrochemical (EC) potential window normally expected by bulk Pourbaix diagrams. Recently, it has been documented that in the case of graphene (Gr), the archetypal 2D material, an EC transfer effect occurs in the oxygen evolution reaction (OER): a single Gr layer, which is *per se* electrochemically inert, can mimic the typical chemical activity of the underlying support, Co_3O_4, as a result of a charge transfer between the two materials[4]. Similarly, the hydrogen adsorption energy on monolayer MoS_2 can be precisely tuned by choosing conveniently the work function of the supporting metal, and so the activity towards the hydrogen evolution reaction (HER) can be substantially boosted[5]. Recently, some of us have demonstrated that 2D nano-oxides, if sufficiently thin (< 2 nm), can exhibit novel EC properties because of the electron tunneling from the underlying metal support[6,7]. Moreover, 2D materials can be chemically modified through the introduction of single atoms forming so-called single atom catalysts (SACs, see Scheme 1c), characterized by unconventional coordination and electronic structure, which are often endowed with rather unique chemical activity[8].

Such great interest in 2D materials and related nanoscale phenomena is motivating the development of novel characterization techniques for their study under *operando* conditions,

possibly with the ability to investigate (electro)catalytic processes with atomic scale precision. This is an ambitious goal considered the substantial dearth of experimental techniques that allow micro-spectroscopic measurements in the complex, and often harsh, environment typical of the working conditions used in (electro)catalytic applications. Most *operando* techniques such as X-ray absorption or vibrational spectroscopies lack sub nanometric resolution, while techniques with atomic resolution such as electron microscopies can be used only for *pre-* and *post mortem* characterization, but not during electrochemical processes.

In the context of electrocatalysis, electrochemical scanning tunneling microscopy (EC-STM) has taken a special standing, since it has been widely exploited in the past to obtain structural and chemical information under *operando* conditions and to provide an atomically resolved picture of several dynamic processes e.g. deposition, dissolution, adsorption/desorption,[9–11] phase transitions[12,13] and surface reactions[14–17].

More recently, EC-STM has also demonstrated the capability to provide a direct visualization of electrocatalytic processes in real time even at the atomic scale[18,19], offering a powerful tool to establish accurate structure-activity relationships in catalysis.

In this work we go beyond the state of the art of this technique, both providing a method for the quantitative analysis of the catalytic activity and reaching high spatial resolution, down to the atomic level of a family of metal-graphene active sites. As firstly recognized in the early development of STM by G. Binning, under certain assumptions, the noise in the tunneling current can be associated with surface dynamical processes. Taking the cue from this intuition, we have developed a method to extract quantitative information from the noise in the tunneling current and to correlate it with the faradaic processes taking place on single atomic sites.

To reach this goal, we have prepared highly-precise model systems consisting of a Gr monolayer covering either a (111) oriented Pt single crystal (Gr/Pt(111)), or few monolayer (ML) Fe films on Pt(111) (Gr/Fe (n ML)/Pt(111)). Thanks to atomically resolved EC-STM images, we have monitored the H^+ intercalation underneath the Gr layer, its adsorption on the metal surface and successive conversion to H_2. Interestingly, through the combination of model systems with the extraordinary capabilities of EC-STM to trace with atomic scale precision in real time nanoscale phenomena, we have demonstrated that the macroscopic electrocatalytic activity, observed in standard linear sweep voltammetry (LSV) experiments, is not only connected to the presence of the Gr/Fe interface, but is also the result of extremely active defects, such as carbon vacancies

filled by Fe atoms, and bent Gr layers, covering like a carpet metal step edges. State-of-the-art density functional theory (DFT) calculations have been used to model the investigated systems, to identify the different defects and to rationalize their catalytic activity, providing an detailed insight into the HER at the atomic level.

2. Results

2.1. Chemical and structural characterization of the Gr/Pt(111) and Gr/Fe (n ML)/Pt(111) model systems.

The growth of both Gr and Fe ultrathin films on Pt(111) was thoroughly studied in the past[20–23]. Some of us investigated the Fe/Gr interface both as supported Fe nanoparticles (Fe/Gr/Pt(111)) and intercalated Fe layers of different thickness (hereafter Gr/Fe(n ML)/Pt(111))[24]. This was possible given the easy intercalation of Fe atoms through Gr, which can be promoted by a mild thermal treatment of the Fe/Gr/Pt(111) system.

In the present study, the atomic structure and chemical composition of the Gr/Pt(111) and Gr/Fe(n ML)/Pt(111) systems have been investigated by LEED and XPS. The results are extensively reported in Supplementary Figures 1 and 2.

Briefly, in the used conditions, Gr grows as a continuous monolayer on the Pt(111) surface, mostly forming a (3 × 3) Moiré superstructure with respect to the Gr periodicity. This film is characterized by a sharp C 1s peak centered at a binding energy (BE) of 284.2 eV that can be fitted by a single component representing C sp^2 atoms[24] (see Supplementary Figure 2a and Supplementary Table 1). After the deposition of 1.2 ML of Fe, directly on Gr/Pt(111) at 570 K to allow an immediate intercalation, three new components appear in the C 1s spectrum: the peak at 284.4 eV can be associated with C sp^2 bonds at the Gr/Fe interface, the component at 285.0 eV with sp^3 rehybridized C atoms, due to defects produced by the Fe deposition/intercalation or to highly bent Gr at step edges[24], and the feature at 283.8 eV, which becomes more evident after a mild sputtering procedure with Ar^+ (0.4 keV for 10 s), is related to C vacancies *(vide infra)*. The shift by 0.2 eV of the C sp^2 peak centroid towards higher BE compared to the same peak observed on the Gr/Pt interface, reflects the stronger cohesive energy between Gr and Fe[24].

This analysis is confirmed by the DFT calculations: Figure S3 (a and b) shows the optimized geometry (top and side views) of the Gr/Pt(111) and Gr/Fe (1 ML)/Pt(111) systems, respectively.

An adsorption energy of -0.08 eV per C atom is calculated in the case of the Gr/Pt interface, in agreement with the literature[25]. However, in the case of Gr/Fe (1 ML)/Pt(111), it increases up to -0.20 eV per C atom. Furthermore, the stronger interaction between Gr and the Fe layer is evident by their interlayer distance, which is reduced from 3.29 Å in Gr/Pt(111) to 2.05 Å in Gr/Fe (1 ML)/Pt(111), and from the analysis of the Löwdin charges, which indicates an additional electron charge transfer of 0.039 e^- per C atom of Gr in Gr/Fe (1 ML)/Pt(111) with respect to that in Gr/Pt(111)[24]. Another proof of the strong change in the interaction between Gr and the two different metals can be deduced by the projected density of states (PDOS) (Figure S4). In the case of Gr/Pt(111) the Dirac cone is almost intact, indicating that Gr is free-standing-like, whereas in the case of Gr/Fe (1 ML)/Pt(111), the Dirac cone is modified because of the mixing of the π states of Gr and the 3d-states of Fe atoms.

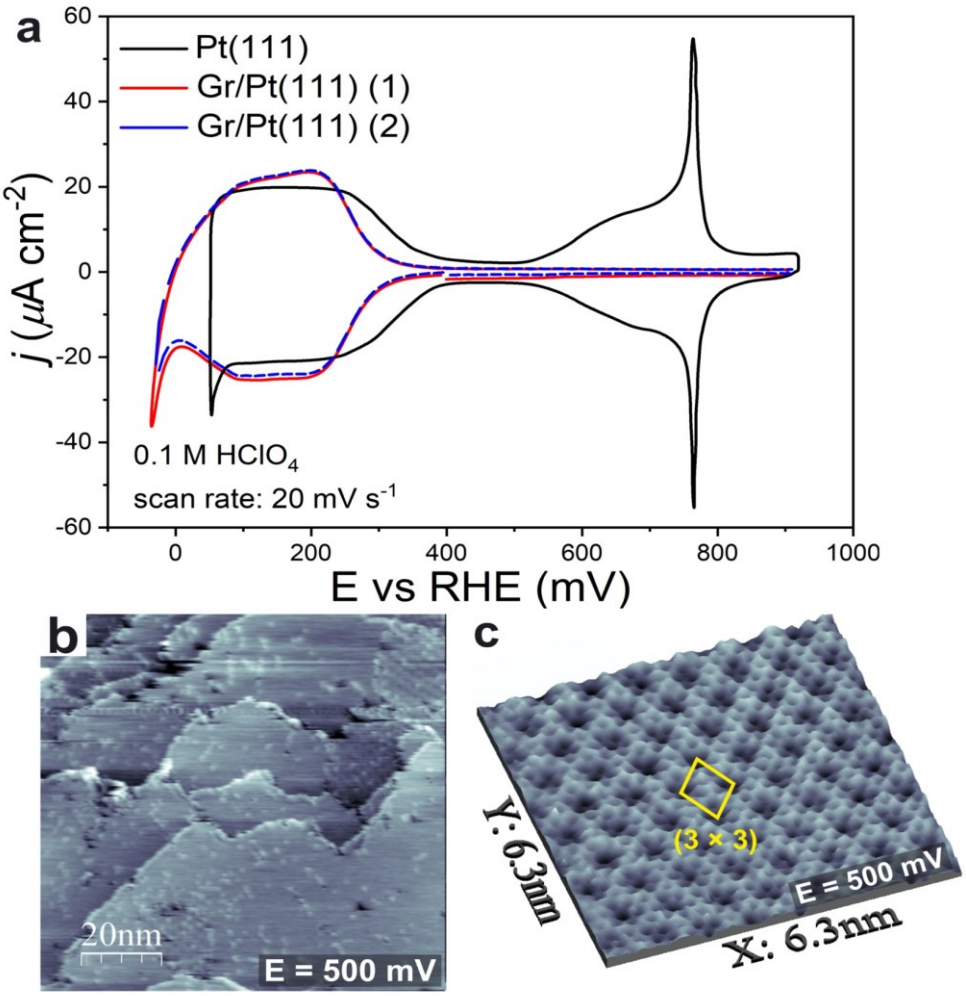

Figure 2. (a) CVs of Pt(111) and Gr/Pt(111) in Ar saturated 0.1 M $HClO_4$ electrolyte: (1) first CV, (2) CV recorded after 72 h by keeping the sample under constant electrode potential (0.5 V vs RHE). Large scale (b) and high-resolution (c) EC-STM images showing the (3×3) Moirè superstructure of Gr/Pt(111) recorded at E =500 mV vs RHE in Ar saturated 0.1 M $HClO_4$ electrolyte, tunnelling conditions: I_t = 0.85 nA, U_b = 78 mV.

2.2 Electrochemical activity towards HER

We first examined the HER activity of the Gr/Pt(111) system and its stability by *in situ* EC-STM measurements in Ar saturated 0.1 M $HClO_4$ electrolyte. Figure 1a shows a typical cyclic voltammogram (CV, red curve) of Gr/Pt(111). As previously reported,[26] anion (OH^-) adsorption/desorption peaks are not observed, suggesting that Gr fully covers the Pt(111) surface; conversely, hydrogen adsorption/desorption peaks (hydrogen underpotential deposition, H_{UPD}) are observed, but shifted by 50 mV towards more negative potentials compared to bare Pt(111) (black

curve in Figure 1a). The integration of the H_{UPD} peak of Gr/Pt(111) yields a charge density of ≈220 μC/cm^2, which corresponds to a monolayer of adsorbed atomic hydrogen[26].

The stability of Gr/Pt(111) in the electrode potential window between 0 and 900 mV was monitored by *in situ* EC-STM: the CV (blue dashed trace in Figure 1a) recorded after 72 h under the constant electrode potential (0.5 V vs RHE) in Ar saturated electrolyte is identical to that recorded at the beginning (red curve in Figure 1a). As to the morphology, large-scale EC-STM images acquired at 500 mV vs RHE (Figure 1b) reveal wide terraces fully covered by the Gr layer with a wide distribution of the Gr domain size (from 20 nm up to 300 nm). High-resolution EC-STM images at 500 mV vs RHE (Figure 1c) reveal a (3×3) Gr superstructure with a periodicity of 7.4 Å and a rotation of 19.1° with respect to the Pt lattice. The surface was continuously monitored by EC-STM and no morphological changes were observed in the double layer potential window (i.e. in the range between 400 mV and 900 mV vs RHE). On the other hand, when STM images (see Figure 2a) were acquired in the potential region of hydrogen adsorption, we observed a (1×1) Gr structure indicating the lift of the (3×3) superstructure caused by hydrogen adsorption directly on the Pt(111) surface, underneath the Gr layer. This process was found to be reversible with respect to the applied EC potential. Figures 2a-b show atomically resolved potentiodynamic STM images registered on the same surface position (indicated by the red arrow in Figure 2a-b). At 0 mV vs RHE a full monolayer of hydrogen is adsorbed on Pt(111) underneath the Gr layer. This proton intercalation process is revealed by a significant change in the corrugation of the Gr layer, which becomes flatter and characterized by a simple (1×1) unit cell. On the other hand, when the applied electrode potential is set in the potential window corresponding to the desorption of hydrogen, the (3×3) pattern immediately reappears.

Since the penetration of protons and hydrogen atoms through a free-standing Gr layer, likely assisted by intrinsic defects, was confirmed by previous DFT calculations and experiments[27,28], in this work we assumed models where hydrogen atoms are adsorbed on the underlying metal substrate. The simulated STM images of Gr/Pt(111) and Gr/H (1 ML)/Pt(111) (where 1 ML indicates the adsorption of seven H atoms per cell on the Pt(111) surface, see Methods section) are shown in Figure 2c-d, respectively. The top and side views of their optimized configurations are shown in Figure 2e-f. The simulations confirm the experimentally observed changes of STM contrast and periodicity upon H intercalation in the confined space between Gr and Pt(111). Interestingly, the defects observed on the images (see yellow circles in Figure 2a and b) undergo

a huge contrast change as a function of the EC potential, being dark at 500 mV, whereas they become very bright and bulged at 0 mV. Our simulated STM images in Figure S5 show that when H_2 molecules physisorb on the Pt(111) surface they appear as bright and bulged features (Figure S5b), whereas chemisorbed H atoms are relatively dark (Figure S5a). Therefore, the bright features observed in the experiments can be interpreted as the H_2 molecules evolving from a cluster of C vacancies (or small vacancy island) amidst the Gr layer, exposing a small patch of Pt(111), where the HER can freely take place.

Considering the literature data on the behavior of Gr covered metal surfaces in other reactions, a rather complex scenario is emerging: in the case of the oxygen reduction reaction (ORR) or oxygen evolution reaction (OER) occurring on Gr wrapped metal or metal oxide surfaces, the active layer is the outer Gr surface, which becomes active because of a strong interfacial hybridization[29]. On the contrary, in the case of the HER, the EC reaction can take place also in the confined space between the metal and Gr.[30]

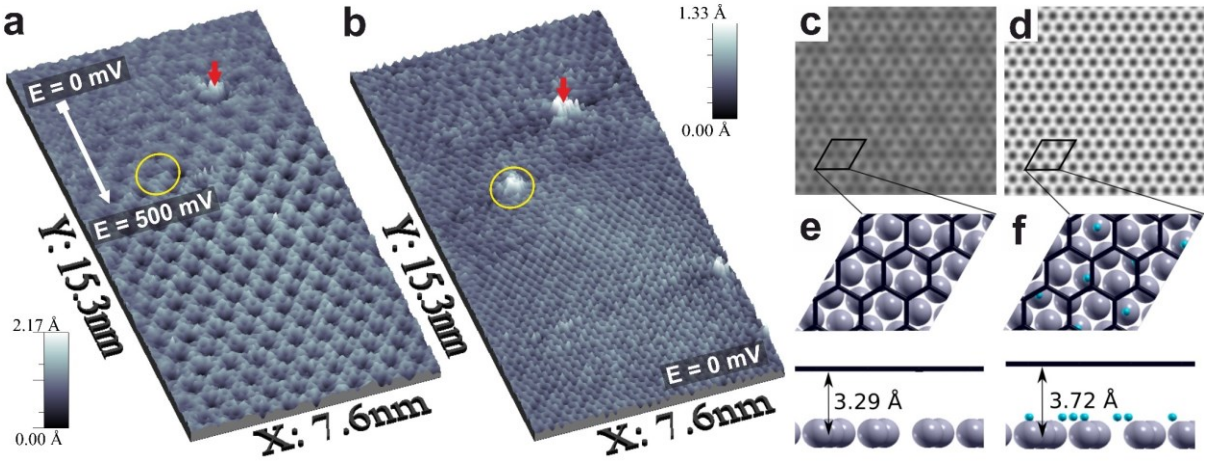

Figure 2. Potentiodynamic EC-STM images (a-b) of Gr/Pt(111) showing the lift of the (3×3) Gr superstructure upon hydrogen adsorption on Pt(111) underneath the Gr layer. In both STM images, the red arrow marks the same point on the surface. (a) desorption of hydrogen: upper part of the image recorded at 0 mV vs RHE and subsequently changed electrode potential to 500 mV vs RHE (lower part of the STM image); tunneling conditions: I_t = 0.85 nA, U_b = 78 mV. (b) STM image recorded at 0 mV vs RHE in 0.1 M $HClO_4$; Constant height simulated STM images at 78 meV and 2 Å for (c) Gr/Pt(111), and (d) Gr/H (1 ML)/Pt(111). The top and side views (only the first layer Pt atoms are shown in the side views) of their optimized geometries are shown in (e) and (f), where graphene is depicted by black sticks, hydrogen and Pt by blue and grey spheres respectively.

Concerning the activity of Pt(111) and Gr/Pt(111) in H_2-saturated 0.1 M $HClO_4$, the LSV data indicate a marked decrease in the catalytic current both for the HER and hydrogen oxidation reaction (HOR) (see Figure 3a), suggesting that Gr strongly suppresses the electrocatalytic performance.

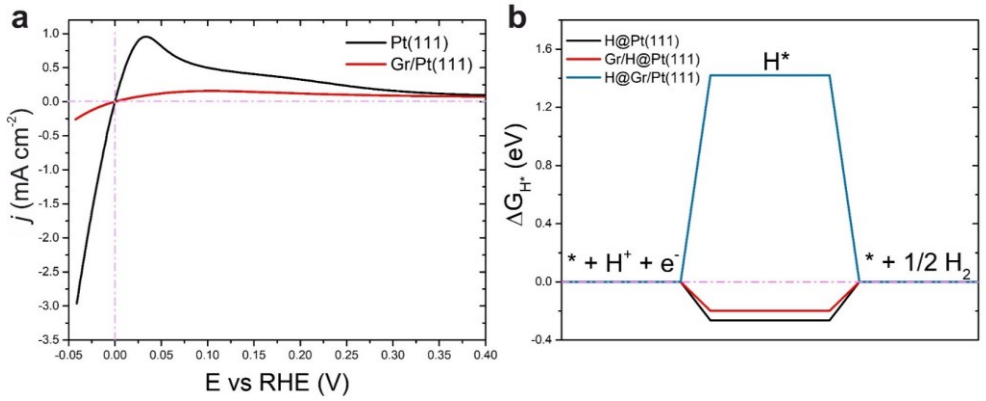

Figure 3. (a) LSV in H_2-saturated 0.1 M $HClO_4$ of the Pt(111) and Gr/Pt(111) electrodes, scan rate 5 mV s^{-1}; (b) Gibbs free energy diagram for hydrogen adsorption on Pt(111), Gr/H@Pt(111), H@Gr/Pt(111) for a single H per unit cell (see Figures S7a, S7b, and S7e for the optimized geometries).

The exchange current density (j_0), which reflects the intrinsic activity of materials is determined from the so-called Tafel plot (see Figure S6) with the value of 0.84 mA cm^{-2} for Pt(111), in accordance with the values reported previously[31,32], and a value of 0.26 mA cm^{-2} for Gr/Pt(111) (see Table S3). These results, however, are apparently in contrast with the results of our DFT calculations, where we modelled the adsorption of H at different coverages from 1/7 to 1 ML (see SI for the optimized structures when a single H is adsorbed on the bare Pt(111) surface (H@Pt(111) in Figure S7a), at the interface between Gr and Pt (Gr/H@Pt(111) in Figure S7b), and on top of the Gr layer supported on Pt (H@Gr/Pt(111) in Figure S7e)). Before examining the DFT results, it has to be reminded that according to the literature the j_0 can be directly compared to the Gibbs free energy of hydrogen adsorption, which is unanimously used as the best descriptor for the HER activity[20,21].

In the case of the lowest coverage, the adsorption of hydrogen on the outer Gr surface is strongly unfavorable (ΔG_{H^*} = +1.42 eV for H@Gr/Pt(111)), whereas in the confined space between Gr and Pt(111) (ΔG_{H^*} = -0.20 eV for Gr/H@Pt(111)), the hydrogen adsorption is exergonic. Interestingly, the presence of Gr slightly destabilizes the adsorption of hydrogen compared to the case of bare Pt(111) (ΔG_{H^*} = -0.27 eV for (H@Pt(111)), therefore producing a

potentially beneficial effect on the catalytic activity, since the highest activity should be observed in correspondence of a thermoneutral ($\Delta G_{H^*} = 0$ eV) adsorption.

The apparent discrepancy with the experimental data can be reconciled if we consider the effects derived by the chemically selective permeation through Gr of the different species involved in the reaction. As a matter of fact, while protons, given their small size, can easily permeate Gr likely through point defects (vacancies, Stone-Wales defects) or even bent areas close to step edges[26,33–35,41] as demonstrated by our EC-STM measurements and other theoretical works; on the contrary the produced H_2 molecules cannot, but have to diffuse underneath Gr to reach large defects such as those present in Figure 2a-b (see yellow circle) or grain boundaries, to be evolved. The resulting entrapment of the H_2 molecules within the confined space between Gr and the metal surface is likely responsible for the observed lower activity of the Gr/Pt(111) system observed in the LSV experiments. On the other hand, the Tafel slopes (Figure S6) of Gr/Pt(111) and Pt(111) are very similar, indicating no significant changes in the HER mechanism, because the reaction takes place in both cases directly on the Pt(111) surface.

When Fe, a metal with a rather scarce activity for HER and with limited stability at the pH and potential conditions mostly used for this reaction (E< 0 V vs RHE and acidic pH), is intercalated underneath the Gr layer, we observe a radical change in the catalytic activity compared to the Gr/Pt(111) system. Figures 4a-b show the CVs of Pt(111) (black), Gr/Pt(111) (red), Gr/Fe (0.6 ML)/Pt(111) (blue), Gr/Fe (1.2 ML)/Pt(111) (green), Gr/Fe (3.5 ML)/Pt(111) (orange) and mildly sputtered (0.4 keV for 10 s) Gr/Fe (3.5 ML)/Pt(111) (light blue) recorded in Ar saturated 0.1 M $HClO_4$ at a scan rate of 20 mV/s are reported. First of all, in all the Gr/Fe/Pt systems no OH^- adsorption/desorption peaks are observed indicating that Gr covers the whole surface and hence Pt is not directly exposed to the electrolyte solution. Moreover, the comparison of the CVs of Gr/Fe/Pt(111) and Gr/Pt(111) indicates significant differences in the H_{UPD} process, consisting of a decrease in the corresponding charge density as a function of the Fe amount (see Table S2): since hydrogen does not adsorb on the Fe surface in the electrode potential window investigated here[36], the charge density calculated from the CVs directly corresponds to the Pt area not covered by Fe. Therefore, the change in the H_{UPD} charge density allows monitoring the Fe coverage directly by CV measurements. In fact, as reported previously, the growth of Fe on Pt(111) proceeds in a

Stranski-Krastanov mode, i.e. forming an interfacial fully wetting monolayer followed by 3D islands, as confirmed by our STM images (vide infra) and by previous works[23,24,37].

Figure S8 shows a CV of Gr/Fe (0.6 ML)/Pt(111) recorded after the contact with the electrolyte (green curve) and after 72 h (blue curve) (under the constant electrode potential of 0.5 V vs RHE): the calculated H_{UPD} charge densities are essentially the same, suggesting that the Gr layer efficiently protects Fe from leaching. This is a notable and unexpected result considering the bulk Pourbaix diagram of Fe, it is however in agreement with previous investigations on powder catalysts made up by Fe nanoparticles coated by a single C layer and supported on single walled nanotubes[38]. The stability of Gr/Fe (0.6 ML)/Pt(111) was further confirmed by EC-STM measurements. Figure S9 reports a series of typical large-scale EC-STM images of Gr/Fe (0.6 ML)/Pt(111) recorded either after the sample was introduced in the EC cell (Figure S9a, open circuit potential (OCP) conditions) or after applying a specific electrochemical potential (Figure S9b,c). The STM topography acquired at the OCP reveals large terraces with Gr encapsulated monoatomic Fe islands with size between 4 and 30 nm. Moreover, no changes of morphology are observed as a function of time, up to an applied electrode potential of +500 mV vs RHE, confirming the stability of the Fe layer.

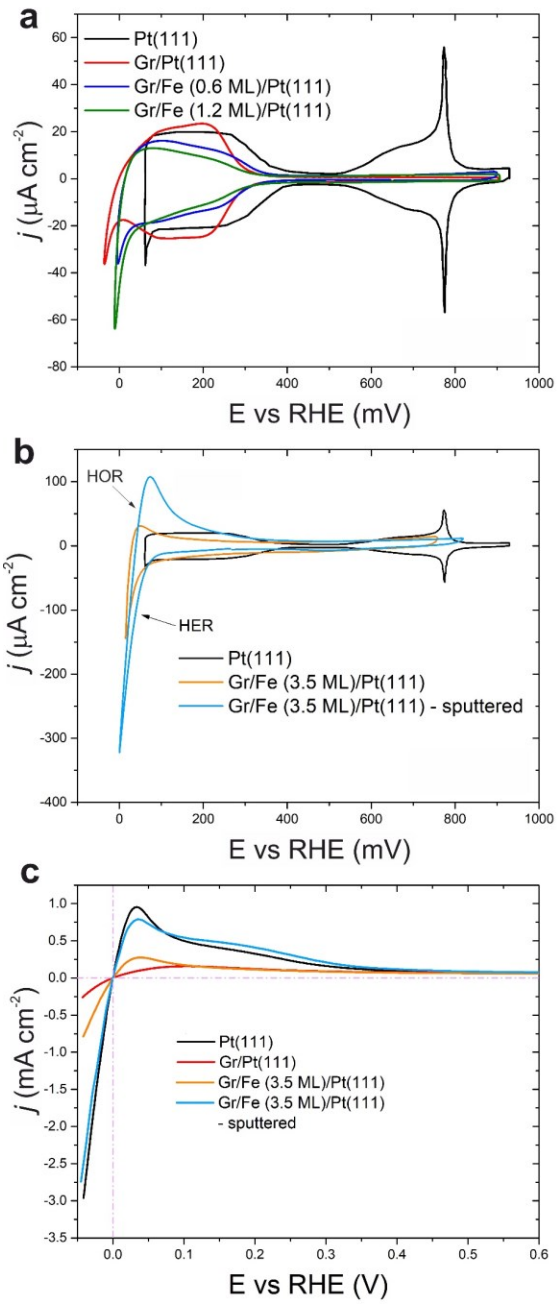

278

279 **Figure 4**. (a-b) CVs of Pt(111) (black), Gr/Pt(111) (red), Gr/Fe (0.6 ML)/Pt(111) (blue), Gr/Fe
280 (1.2 ML)/Pt(111) (green), Gr/Fe (3.5 ML)/Pt(111) (orange) and mildly sputtered Gr/Fe (3.5
281 ML)/Pt(111) (light blue) recorded in Ar-sat. 0.1 M $HClO_4$ electrolyte with the scan rate of 20 mV
282 s^{-1}; (c) LSV in H_2-saturated 0.1 M $HClO_4$ of the Pt(111) and Gr/Pt(111) electrodes, scan rate 5 mV
283 s^{-1}.
284

285 When a high coverage (>3 ML) of Fe is intercalated, a rough metal film characterized by 3D
286 islanding growth mode can be observed as reported in the EC-STM investigation of Gr/Fe (3.5
287 ML)/Pt(111) (Figure S10). Even in this case we were able to acquire atomically resolved images

showing the presence of a variety of bright defects that can be associated with either C vacancies or Fe atoms trapped into defects (single or multiple vacancies within the Gr layer)[39]. The presence of such defects is confirmed also by the analysis of the C 1s photoemission spectrum of the Gr/Fe (3.5 ML)/Pt(111) sample (Figure S2a), which shows an additional component at 283.8 eV (separated from the main peak by -0.6 eV) compatible with the presence of C vacancies and/or Fe-C bonds. This component further increases after a mild Ar^+ sputtering, which is a treatment known to produce C vacancies, confirming the correctness of the attribution. Moreover, we have simulated the photoemission spectra (Figure S2b) of a double C vacancy (2V) either empty (i.e. 2VGr/Fe (3 ML)/Pt(111)) or trapping an Fe atom (i.e. Fe-2VGr/Fe (3 ML)/Pt(111)), and found that the C atoms at the 2V produce a photoemission peak shifted by -0.8 eV or -0.6 eV, respectively, compared to that of the C sp^2 component.

Furthermore, atomically resolved EC-STM images (Figure S10c and S10d) supported by DFT simulations (Figure S10e), as it will be discussed in detail in the following, allow identifying C double vacancies (2V) filled by an Fe atom forming Fe-C_4 rectangular units, characterized by a rather bright contrast in the EC-STM images. Taking into account that this set of STM images have been recorded after 30 CVs in potential range between 0 mV and 500 mV vs RHE and after 24 h by keeping the sample under a constant electrode potential (0.5 V vs RHE) in Ar saturated 0.1 M $HClO_4$, we can conclude that Fe atoms cannot leach through Gr point defects, because either they get trapped in the defect itself or because of the strong adhesion energy within the Fe layer. It should be mentioned however, that a small amount of Fe could leak just after the contact with the electrolyte. Indeed in the CV data (Figure S11 and Table S2) of the Gr/Fe (3.5 ML)/Pt(111) sample after a mild sputtering treatment, a small current wave is observed in the potential range between 0 and 300 mV vs RHE. This feature can be connected to H_{UPD} at the interface between Gr and the Pt surface. The calculated charge density is 14 $\mu C/cm^2$, which corresponds to 6 % of Pt areas not covered by the Fe layer. These data suggests that Fe can partially dissolve into the electrolyte, but according to EC-STM measurements this process cannot take place through point defects, but likely through grain boundaries or other larger morphological defects.

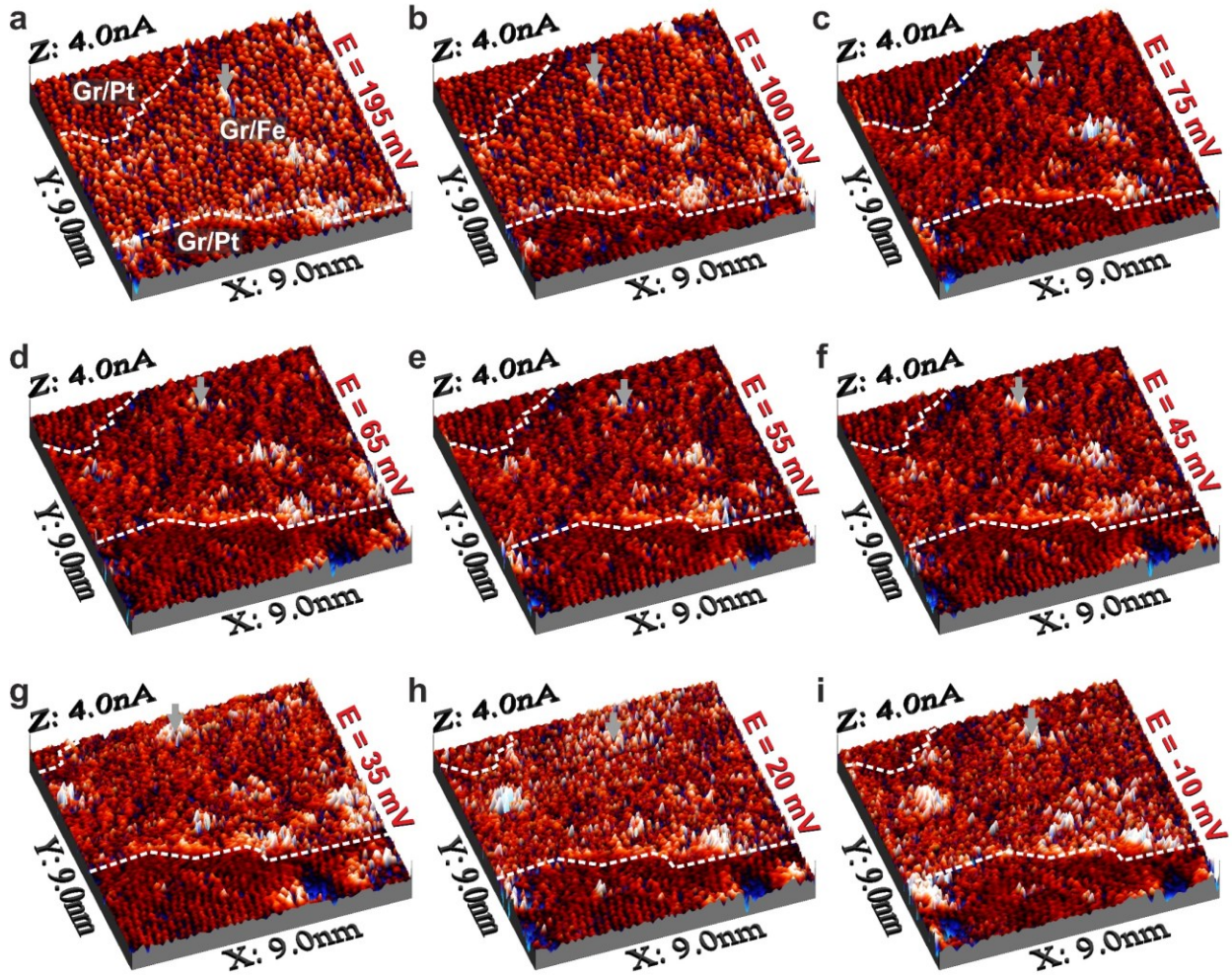

Figure 5. Potentiodynamic EC-STM images in current mode of catalytic activity of Gr/Fe (1.8 ML)/Pt(111);(a-i) tunneling conditions: I_t = 1.50 nA, U_b = -16 mV. The grey arrow always indicates the same position on the surface. The white dashed lines in panels (a-i) marks step edges between Gr/Pt-Gr/Fe and Gr/Fe-Gr/Pt basal planes.

Once evaluated the long-term stability of the Gr/Fe system, we focused on the catalytic performance. Surprisingly, the CV and LSV data (Figure 4) clearly indicate that the Gr/Fe interface is more reactive than the Gr/Pt one, reaching almost the same activity of the bare Pt(111) surface (see Table S3 and Figure S12). Besides, the HER activity is dependent on the amount of Fe, with thicker layers being more active. This can be connected to the increasing number of point defects observed at higher coverage and with the formation of a rough surface with several step edges as deduced by XPS and STM measurements. Therefore, in order to get an insight at the atomic level

329 into the catalytic activity and stability of the Gr/Fe system and directly compare it to the Gr/Pt
330 interface we performed a potentiodynamic STM study (see Figure 5 and S13 for current and
331 topography mode, respectively) from pre-catalytic conditions to more reducing conditions for
332 Gr/Fe (1.8 ML)/Pt(111), which allows observing on the same surface both Gr/Fe and Gr/Pt
333 patches. The series of images reported in Figure 5 is part of a potentiodynamic experiment (68
334 STM images in total) that is presented in Supplementary Movie 1 (where an extended description
335 of the movie can also be found - Figure S14).
336 To analyze the data of the potentiodynamic experiments we have followed an approach that
337 represents an implementation of a technique originally proposed by Bandarenka et al..[18] This
338 innovative method allows investigating in a quantitative way the electrocatalytic activity of
339 different chemical and morphological defects, which can be identified in atomically resolved STM
340 images. Some technical details of this method are reported in the following and in the SI, whereas
341 its full description will be the object of a forthcoming publication. The current images reported in
342 Figure 5 show an apparent progressive loss of the atomic resolution as the EC potential is reduced;
343 however, this phenomenon is not due to instrumental factors, such as a modification of the tip or
344 mechanical instabilities etc., but is the consequence of the applied EC potential since it is highly
345 reversible with respect to it (see Figure S16). Nonetheless, it can be observed that these changes
346 in the resolution do not affect in the same way the whole surface, but in some regions, such as step
347 edges and point defects, occasional spikes and noise are particularly enhanced. As suggested in
348 the seminal work by Bandarenka et al.[18], such instabilities of the tunneling current are due to
349 instantaneous variations of the tunneling resistance due to changes of the local environment
350 triggered by an EC reaction, and therefore represent a powerful tool for the identification of active
351 sites. In Figure 6a, which is a simple 2D topography of the same area shown in Figure 5, we can
352 recognize several different structural situations: patches of Gr covering the basal plane of a Fe
353 island (Gr/Fe), or directly in contact with the Pt substrate (Gr/Pt) and the corresponding step edges.
354 Moreover, several types of point defects made up by a different number of missing C atoms and
355 trapped Fe atoms are visible, such as one Fe atom trapped on two (Fe-2V), three (Fe-3V) or four
356 (Fe-4V) adjacent C vacancies, and three Fe atoms trapped into a cluster of 6 C vacancies (3Fe-
357 6V). As discussed in the following, the most notable of these structures have been simulated by
358 DFT calculations (see Table S4 and Figure S21).

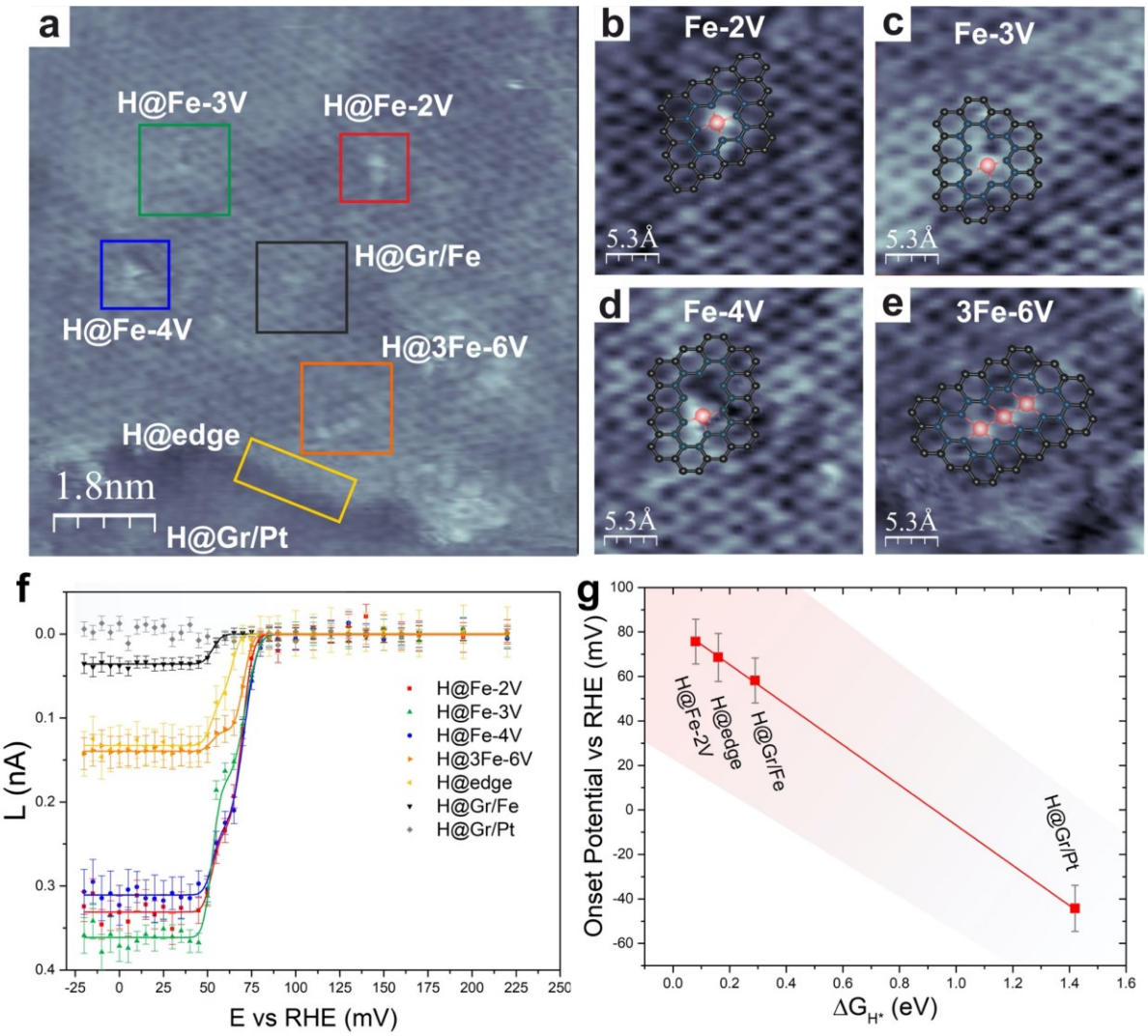

Figure 6. (a-f) EC-STM topographic images of the Gr/Fe (1.8 ML)/Pt(111) surface recorded at E = 195 mV vs RHE, tunneling parameters: I_t = 1.50 nA, U_b = -16 mV; f) Normalized current roughness L as a function of the EC potential extracted from the areas outlined by the rectangular boxes in (a); g) Plot of onset potential versus Gibbs free energy of adsorption (ΔG_{H^*}) showing a linear relationship.

To provide a quantitative basis to Bandarenka's original method[18], we introduced a quantity L_o that can be described as current roughness (cr), which is a measure of the deviation of the tunneling current from the set value, due to the fluctuation of the tunneling junction resistance produced locally by the ongoing EC reaction, and is defined as:

$$L_0 = \sqrt{\frac{\sum_{x,y}(I_{x,y}-I_{set})^2}{N}} \cdot \frac{A_{SET}}{A_{SITE}} \quad (1)$$

where: $I_{x,y}$ are the measured current values on an (x_j,y_j) point, I_{set} is the current value set in feedback loop of the EC-STM working in constant current mode, A_{SET} is the area of the portion of the STM image analysed (e.g. the areas of the rectangles in Figure 6a) and A_{SITE} is the actual area of the investigated catalytic site. The technique herein implemented will be referred as cr-EC-STM. The absolute value of L_0 depends on the STM acquisition parameters, local electronic structure, and topographic corrugation; therefore, to enable a comparison, the L_0 values were normalized with respect to a constant K that depends on the difference between the value of the set current, I_{set} and its average local value, $I_{Average}$ and assuming as reference zero the value of L_0 at an electrochemical potential when the reaction is off, L_0(off). More details are provided in the SI. The normalized quantity L(E) (see Supplementary Equation 3) can be calculated on rectangular areas enclosing different points of interest and plotted as a function of the EC potential (Figure 6f).

Interestingly, the general shape of the plot of L(E) vs EC potential is very similar to LSV data. This can be easily explained assuming that the catalytic reaction and ultimately the catalytic current is a first order perturbation of the tunneling current measured by EC-STM.

When the onset potential, i.e. the lowest potential where a catalytic current can be detected, for the reaction is reached, the HER starts taking place, producing instantaneous changes in the tunneling junction since protons are continuously reduced to H, and H_2 is formed and desorbed. Therefore, the L(E), which quantifies the roughness or noise in the tunneling current, can be directly associated with the catalytic current. By means of EC-STM, such measurement can be acquired in real time with high spatial resolution*, operando* at different EC potentials. Eventually however, when the overpotential is large enough, the associated noise in the tunneling current reaches a steady value, which explains the plateau observed at more reducing potential.

Therefore, by using the current roughness, cr-EC-STM provides the possibility to investigate with atomic scale precision the catalytic activity of single defects and special structural units, allowing to go beyond the area averaged information provided by standard EC techniques. As in standard LSV, the cr vs voltage plots allow identifying the catalytic sites present on a surface and to determine quantitatively their onset potential (Table 1). The comparative analysis of the L(E) curves of the different sites indicates that the point defects based on Fe atoms trapped into vacancy clusters are the most active sites followed by the iron step edge and the Fe basal plane covered by Gr. This detail in the direct visualization of catalytically active sites during an EC reaction is in

excellent agreement with the results of DFT calculations where the different defects have been simulated (see Table 1).

We started by modelling a Pt(111) surface covered with increasing amount of Fe (from 1 to 3 ML, see Methods section for more details) terminating on top with a Gr layer. In all these cases, the free energy (ΔG_{H^*}) values for a single H adsorption on top of Gr, are slightly exergonic, but strongly dependent on the Fe layer thickness. The system with a single layer of Fe is the most active with a ΔG_{H^*} of +0.29 eV (Figure S7f), whereas at higher coverages (2 and 3 ML), the ΔG_{H^*} saturates at around +0.48 eV (Figures S7g,h). More interestingly, the activity of Gr/Fe (n ML)/Pt(111) is substantially boosted if the Gr layer becomes curved, as it happens on step edges. The Fe step edge has been modelled by a $6\sqrt{7}\times1\sqrt{7}$ supercell consisting of two complete Fe layers on Pt(111) and a third layer of an Fe island with a Gr layer on top, which covers the whole surface in a carpeting mode, assuming a wavy conformation comprising flat and curved regions. The adsorption of H atoms has been tested on several sites on this model (see Figures S18a-d) and, among them, the most favored adsorption energy (ΔG_{H^*} = +0.16 eV) has been found on the C atoms not directly attached to the iron layer, which are located at the curved areas adjacent to the step edges. Notably, in this case the H atom is preferentially adsorbed on top of the Gr layer and not in the confined space between iron and Gr. These values are comparable with other works in the literature dealing with Gr encapsulated metals[8,40].

Table 1. Gibbs free energy for hydrogen adsorption and onset potential determined by the cr-EC-STM method.

	ΔG_{H^*} (eV)	Onset potential vs RHE (mV)
H@Gr/Pt(111)	1.42	-44 ± 10
H@Gr/Fe (1 ML)/Pt(111)	0.29	59 ± 10
Edge of H@Gr/Fe (2.5 ML)/Pt(111)	0.16	69 ± 11
H@Fe-2VGr/Fe (1 ML)/Pt(111)	0.08	76 ± 10

On the bottom of Figure 6a, it is possible to observe also a small area where Gr directly covers the Pt(111) surface as deduced by the height profile, which is in agreement with the DFT

calculations (see Figure S7e). Here, the local current roughness measurements probe the HER that is taking place on the Gr outer surface and not within the confined space. No rise in the current roughness is observed in the potential window investigated here (i.e. up to -25 mV vs RHE). Therefore, to determine the onset potential of the basal plane of Gr/Pt(111), a further potentiodynamic EC-STM experiment has been performed and the results are shown in Figure S19 and in a second movie included in Supplementary Movie 2. For the Gr/Pt(111) system, DFT calculations predict a rather endergonic ΔG_{H^*} of +1.42 eV in excellent agreement with the fact that experimentally the onset of catalytic activity is observed at the most reducing potential (-44 mV vs RHE).

Finally, we modelled some of the point defects that are formed during the intercalation of Fe and that were documented on several areas. We envisaged the formation of C double (2V) vacancies (i.e. removal of two adjacent C atoms): we considered it either as an empty defect or filled by one Fe atom, forming a pseudo square-planar coordination Fe-C_4 unit (Figure S21b-f). In the latter, the Gr layer was supported on 1, 2 and 3 ML Fe films on Pt(111). The simulation of the STM image of such a defect is reported in Figure S10e and nicely reproduces the bright four-fold structure labelled as defect Fe-2V in Figure 6b. On this special defect, hydrogen can adsorb on top of the metal atom with a Gibbs free energy of adsorption ΔG_{H^*} of +0.08 eV (Table S4). In this case the active site is directly exposed to the electrolyte solution providing an easy mass transport for both reactants and products.

The high activity of this type of defects deduced by cr-EC-STM and DFT calculations was independently confirmed by LSV experiments carried out on sputtered surfaces (see Figure 4c). A Gr/Fe (3.5 ML)/Pt(111) surface was gently sputtered by Ar^+ (0.4 keV for 10 s) to form C vacancies, which can be easily metalated by the underlying Fe atoms[41]. LSV recorded in H_2-sat. 0.1 M $HClO_4$ shows that after sputtering, the catalytic activity of the system increases substantially almost matching the activity of the Pt(111) surface.

Overall, the sequence of reactivity experimentally observed by cr-EC-STM therefore perfectly agrees with the trend of ΔG_{H^*} obtained by the DFT simulations, actually if we plot the onset potential points of the L(E) vs EC curves, which is an experimental determination of the overpotential vs ΔG_{H^*} we observe a linear correlation (see Figure 6g).

3. Conclusions

In this work we have investigated the HER at the interface between Gr and two different metals, namely Pt and Fe, unravelling quite different behaviors. In the confined space between Gr and Pt, the HER is thermodynamically boosted (ΔG_{H^*} =-0.20 vs -0.27 eV for clean Pt(111)), but is limited by the diffusion of the H_2 molecules away from the interface. On the other hand, on the outer surface of the Gr/Pt(111) system, the HER is strongly suppressed, given the scarce interaction between the H atoms and Gr (ΔG_{H^*} =+1.42). Moreover, when Fe is intercalated below Gr, producing a Gr/Fe interface, radical changes are observed in the activity and in the reaction mechanism. In this case the large electronic modification induced on Gr by the close contact with the Fe layer allows the reaction to take place directly on the outer Gr surface (ΔG_{H^*} =+0.29 eV). Through the introduction of the local roughness of the tunneling current and an innovative method (cr-EC-STM) for the analysis of the noise in the atomically resolved potentiodynamic EC-STM images, it was possible to investigate under *operando* conditions with sub nanometric resolution, the activity of several different structural units such as point defects, step edges and compositionally different flat interfaces. The converging evidence of DFT calculations and experimental data indicates that the Fe atoms trapped into C vacancies behave as very reactive SACs (ΔG_{H^*} as low as +0.08 eV), and that the activity of the bent areas of Gr across step edges is also remarkable (ΔG_{H^*} of +0.16 eV). This work therefore sheds light on the electrocatalytic activity of metal surfaces wrapped by graphitic layers, which are showing an enormous potential not only in the HER, but also in the ORR and OER[42]. Differently from other works however, we were able to provide both experimental evidences and theoretical models based on DFT calculations that confirm the importance of point defects, which so far have been overlooked in the literature due to the dearth of suitable investigation techniques with high spatial resolution under *operando* conditions. With this work we provide a detailed blueprint for the design of HER catalysts bearing specific types of defects such as Metal-C_4 units and curved Gr, with outstanding activity (ΔG_{H^*} = +0.08 eV) and demonstrate the potential of cr-EC-STM in electrochemistry. In fact, this technique allows to acquire quantitative electrocatalytic measurements with high resolution down to the atomic level. This tool, therefore, can bring a radical change in perspective on the methodological approach used to investigate electrocatalysts. Actually, the biggest conundrum in the field is how to connect the catalytic performance of materials to their atomic scale properties. Cr-EC-STM allows to go beyond the usual area averaged measurements and on the contrary, to break down the

electrocatalytic response of a complex surface, even though it is inhomogeneous and presents a variety of defects, into the single components associated with specific sites. This combination of high spatial resolution and *operando* evaluation of catalytic activity represents a powerful tool to derive accurate structure-activity relationships in electrocatalysis.

4. Methods

The preparation of the Gr/Pt(111) and Gr/Fe/Pt(111) systems and their characterization by Low Energy Electron Diffraction (LEED) and X-ray Photoemission Spectroscopy (XPS) were performed in a custom-designed Ultra-High Vacuum (UHV) system described in Ref[43].

Synthesis of Gr/Pt(111) and Gr/Fe(n ML)/Pt(111) samples. The surface of a Pt(111) single crystal (MaTeck) was cleaned by repeated cycles of sputtering (1.5 keV, 1×10^{-6} mbar of Ar, at room temperature RT) and annealing at 1000 K. The residual carbon was removed by annealing in 2.0×10^{7} mbar of O_2 at 900 K, and subsequently, the adsorbed oxygen was removed by flash heating at 1000 K. This procedure was repeated until a sharp LEED pattern was obtained (Fig. S1a). The Gr/Pt(111) model system was grown *in situ* on the clean Pt(111) surface by ethylene dosing following a previous procedure described by Cattelan et al.[24]**:** the Gr layer was grown *in situ* by ethylene dosing (5×10^{-8} mbar, at 1000 K, for 5 min and subsequently in 1×10^{-6} mbar for 15 min) on the clean Pt(111) surface and then cooling down the crystal at 50 $Kmin^{-1}$.[44] Different Gr/Fe(n ML)/Pt(111) model surfaces (where n indicates the number of monolayers MLs) were then prepared according to a procedure described in the same paper[24]: Fe was deposited *in situ* by physical vapor deposition (PVD) on the Gr/Pt(111) system after a proper calibration of the iron evaporator by angle-resolved XPS (AR-XPS) measurements using the Fe 2p and Pt 4f photoemission peak intensity, according to a method previously described[44]. Fe was evaporated while maintaining the sample at 570 K to allow the metal intercalation, i.e. the diffusion of Fe atoms through the Gr layer, forming metal thin films between the Pt(111) surface and the Gr layer. The thickness of the layer is expressed in terms of monolayer (ML), where 1 ML correspond to 2.60×10^{15} Fe atoms/cm^2.

Chemical and Structural Characterization. The composition of the samples and the chemical changes induced by the exposure to the EC environment were investigated by XPS using an EA 125 Omicron electron analyzer equipped with five channeltrons, working at a base pressure of 2×10^{-10} mbar. The XPS data were collected at RT with the Mg Kα line ($h\upsilon$ = 1256.6 eV) of a non-monochromatized dual-anode DAR400 X-ray source using 0.1 eV energy steps, 0.5 s acquisition time, and 20 eV pass energy. The binding energy (BE) scale was calibrated using a gold sample (Au $4f_{7/2}$ at 84 eV). The curve fitting of the C 1s lines was performed using Voigt functions and a Shirley background using the KolXPD software[45]. LEED patterns were acquired using an incident electron beam energy between 40 and 100 eV. All LEED patterns were recorded at RT.

In situ EC Scanning Tunneling Microscopy Measurements. The *in situ* EC-STM measurements were carried out using a home-built EC-STM operating in constant current mode, as described by

Wilms et al.[46]. The STM tips were electrochemically etched from a 0.25 mm tungsten wire in 2 M KOH solution and, subsequently, cleaned in high purity water, dried and coated passing the tip through a drop of hot glue. Platinum wires were used as counter and reference electrodes in order to ensure a high-purity of the system. The Pt reference electrode was calibrated vs. $Ag/AgCl/Cl_{(sat)}^-$ in Ar-saturated 0.1 M $HClO_4$. The overall error in the EC potential scale was estimated to be 10 mV. The exposed area of the sample during EC-STM measurements was 0.096 cm^2. The image analysis was carried out by using the WSxM 5.0 software[47]. To correct for experimental artefacts (e.g. thermal drift) and for a better visualization, in some cases, the displayed EC-STM images have been subjected to: plane correction, equalization, fast Fourier transform filter, and drift correction based on the Gr lattice. Figure S22 shows a typical raw (not filtered/corrected) EC-STM image obtained in topographic and current mode (raw EC-STM image of Figure 6a). The analysis of the current roughness has been performed on the raw EC-STM images. The error bars reported in the L vs EC potential plots (Fig 6f) were determined on the basis of the standard deviation of the tunneling current values within each rectangular box.

***Ex situ* EC Measurements.** The Linear sweep voltammetry (LSV) measurements in H_2-saturated 0.1 M $HClO_4$ electrolyte of prepared samples were carried out *ex situ* in a conventional three-electrode cell. A glassy carbon rod was used as counter electrode and an $Ag/AgCl/Cl_{(sat)}^-$ as reference electrode. A custom-designed sample holder with an area of 0.502 cm^2 was used in an upside-down configuration causing mass transport limitation at high current densities. Both *for ex situ* and *in situ* measurements, all samples have been introduced in the electrochemical cell without an external bias or connection to a load. Typical values of the open circuit potential were 920 mV for the Pt(111) surface and 810 mV for the Gr covered systems, respectively.

Computational details. DFT was used to study the various systems namely H@Pt(111), Gr/H@Pt(111), H@Gr/Pt(111), Gr/H@Fe (n ML)/Pt(111), H@Gr/Fe (n ML)/Pt(111), and H@Gr/Fe island (n ML)/Pt(111) for different H coverages (not all are shown here). We also investigated H adsorption at the single (1V) and double vacancies (2V) in Gr for the systems with Fe. The Quantum Espresso suite was used to model and simulate the systems[48] and the Tersoff-Hamann approach was used to simulate the STM images[49]. Ultrasoft pseudopotentials requiring wave function and charge density cut-offs of 46 Ry and 401 Ry were used, respectively. From the Moiré-like pattern observed in the experimental EC-STM images, as the majority phase of Gr/Pt(111) was determined to be a (3×3) Gr on (√7×√7)R19.1° Pt(111), the same was modelled using the repeated slab approach. The lattice mismatch between Gr and Pt(111) is of 0.6 %. This mismatch cannot be modeled due to the periodic boundary conditions used in simulations. Hence, we stretched the Pt substrate to match the Gr lattice. However, we made sure that the properties of the Pt substrate were unaltered by this negligible increase in the lattice constant by checking the work function. The calculated work function of the stretched Pt(111) slab is 5.92 eV which agrees with the value in the literature[50]. The Pt slab consists of four layers where the bottom two layers were kept fixed during all relaxations. For the systems with Fe (1 ML or less), Fe atoms were

added on top of the Pt substrate. For Fe (2 ML or more) systems, the same number of Pt layers were replaced with the Fe layers (see Figure S7). As there are seven substrate-surface atoms per cell, the full-coverage equivalent of 1 ML in simulations is when seven atoms are present. A 12×12×1 Monkhorst-Pack[51] k-points grid was used to sample the Brillouin zone. To include the van der Waal's interactions, all calculations were run including the vdW-DF2^{c09x} non-local functional[52–55].

To model the EC half-cell we used the computational hydrogen electrode (CHE) model developed by Nørskov and co-workers[56]. The electronic energy of atomic hydrogen adsorption (ΔE_{H*}) is calculated as: $\Delta E_{H*} = 1/n\ (E_{surf+nH} - E_{surf} - n/2\ E_{H_2})$ where $E_{surf+nH}$ is the total energy of the system with *n* number of H atoms adsorbed, E_{surf} is the energy of the slab and E_{H_2} is the energy of the H_2 molecule in the gas-phase. Once we obtain the electronic energy, the Gibb's free energy for atomic hydrogen adsorption ΔG_{H*}, which is the key descriptor of HER used in simulations, was obtained as follows: $\Delta G_{H*} = \Delta E_{H*} + \Delta ZPE_{H*} - T\Delta S_{H*}$, where ΔZPE_{H*} is the zero-point energy difference between the reactants and the products and ΔS_{H*} is the difference in the entropies between them[8]. Vibrational modes were calculated by performing a normal-mode analysis and all 3N degrees of freedom of the adsorbates within the harmonic oscillator approximation. Corrections for the ZPE were included by calculating and diagonalizing the dynamical matrix at Γ point only. For a gas-phase H_2 molecule, the standard tabulated entropy was used. The more negative the ΔG_{H*} value is, the stronger is the adsorption and a positive value indicates non-bonding, or a very weak adsorption. The best catalyst should have the ideal value of $\Delta G_{H*} \approx 0$ eV. However, it is worth to underline how a thermoneutral hydrogen adsorption step is a necessary but not sufficient condition for a catalyst to be active for HER.

The C 1s XPS was simulated by determining the core level shifts (CLS) between the inequivalent carbon atoms[57]. The CLS were calculated as the total energy differences between the systems with different inequivalent excited atoms and their weighted average. The excited atoms were modelled by a C pseudopotential generated with a full core hole at the 1s level. The final spectra were obtained by broadening the CLS with pseudo-Voigt profiles[58,59]. The ball and stick models have been rendered by using the XCrySDen software[60].

Data availability

The data supporting the findings of this study are available within the article and its Supplementary Information or from the corresponding authors upon reasonable request.

References

[1] L. Calvillo, G. García, A. Paduano, O. Guillen-Villafuerte, C. Valero-Vidal, A. Vittadini, M. Bellini, A. Lavacchi, S. Agnoli, A. Martucci, J. Kunze-Liebhäuser, E. Pastor, G. Granozzi, Electrochemical Behavior of TiOxCy as Catalyst Support for Direct Ethanol Fuel Cells at Intermediate Temperature: From Planar Systems to Powders, ACS Appl. Mater. Interfaces. 8 (2016) 716–725. doi:10.1021/acsami.5b09861.

[2] C.S. Fadley, Angle-resolved x-ray photoelectron spectroscopy, Prog. Surf. Sci. 16 (1984) 275–388. doi:10.1016/0079-6816(84)90001-7.[3] Http://www.kolibrik.net/science/kolxpd/, http://www.kolibrik.net/science/kolxpd/, (n.d.).
[4] M. Wilms, M. Kruft, G. Bermes, K. Wandelt, A new and sophisticated electrochemical scanning tunneling microscope design for the investigation of potentiodynamic processes, Rev. Sci. Instrum. 70 (1999) 3641. doi:10.1063/1.1149971.
[5] I. Horcas, R. Fernández, J.M. Gómez-Rodríguez, J. Colchero, J. Gómez-Herrero, A.M. Baro, WSXM : A software for scanning probe microscopy and a tool for nanotechnology, Rev. Sci. Instrum. 78 (2007) 1–8. doi:10.1063/1.2432410.
[6] M. Cattelan, G.W. Peng, E. Cavaliere, L. Artiglia, A. Barinov, L.T. Roling, M. Favaro, I. Píš, S. Nappini, E. Magnano, F. Bondino, L. Gavioli, S. Agnoli, M. Mavrikakis, G. Granozzi, The nature of the Fe-graphene interface at the nanometer level, Nanoscale. 7 (2015) 2450–2460. doi:10.1039/c4nr04956j.
[7] Y. Fu, A. V. Rudnev, G.K.H. Wiberg, M. Arenz, Single Graphene Layer on Pt(111) Creates Confined Electrochemical Environment via Selective Ion Transport, Angew. Chemie - Int. Ed. 56 (2017) 12883–12887. doi:10.1002/anie.201705952.
1. Deng, D. *et al.* Catalysis with two-dimensional materials and their heterostructures. *Nat. Nanotechnol.* **11**, 218–230 (2016).
2. Sun, P. Z. *et al.* Limits on gas impermeability of graphene. *Nature* **579**, 229–232 (2020).
3. Fu, Q. & Bao, X. Surface chemistry and catalysis confined under two-dimensional materials. *Chem. Soc. Rev.* **46**, 1842–1874 (2017).
4. Sharifi, T. *et al.* Graphene as an electrochemical transfer layer. *Carbon* **141**, 266–273 (2019).
5. Chen, W., Santos, E. J. G., Zhu, W., Kaxiras, E. & Zhang, Z. Tuning the electronic and chemical properties of monolayer MoS2 adsorbed on transition metal substrates. *Nano Lett.* **13**, 509–514 (2013).
6. Kosmala, T., Calvillo, L., Agnoli, S. & Granozzi, G. Enhancing the Oxygen Electroreduction Activity through Electron Tunnelling: CoO_x Ultrathin Films on Pd(100). *ACS Catal.* **8**, (2018).
7. Kosmala, T. *et al.* Stable, Active, and Methanol-Tolerant PGM-Free Surfaces in an Acidic Medium: Electron Tunneling at Play in Pt/FeNC Hybrid Catalysts for Direct Methanol Fuel Cell Cathodes. *ACS Catal.* **10**, 7475–7485 (2020).
8. Baby, A., Trovato, L. & Di Valentin, C. Single Atom Catalysts (SAC) trapped in defective and nitrogen-doped graphene supported on metal substrates. *Carbon* **174**, 772–788 (2021).
9. Itaya, K. & Tomita, E. Scanning Tunneling Microscope For Electrochemistry - A New Concept For The In Situ Scanning Tunneling Microscope In Electrolyte Solution. *Surf. Sci. Lett.* **201**, L507–L512 (1988).
10. Itaya, K. Recent Progresses of Electrochemical Surface Science ~Importance of Surface Imaging with Atomic Scale~. *Electrochemistry* **83**, 21–25 (2015).
11. Madry, B., Morawski, I., Kosmala, T., Wandelt, K. & Nowicki, M. Porphyrin Layers at Cu/Au(111)–Electrolyte Interfaces: In Situ EC-STM Study. *Top. Catal.* **24**, 1335–1349 (2018).
12. Phan, T. H., Kosmala, T. & Wandelt, K. Potential dependence of self-assembled porphyrin layers on a Cu(111) electrode surface: In-situ STM study. *Surf. Sci.* **631**, (2015).
13. Kosmala, T., Blanco, M., Granozzi, G. & Wandelt, K. Potential Driven Non-Reactive Phase Transitions of Ordered Porphyrin Molecules on Iodine-Modified Au(100): An

Electrochemical Scanning Tunneling Microscopy (EC-STM) Study. *Surfaces* **1**, 12–28 (2018).
14. Zuili, D., Maurice, V. & Marcus, P. Surface Structure of Nickel in Acid Solution Studied by In Situ Scanning Tunneling Microscopy. *J. Electrochem. Soc.* **147**, 1393–1400 (2000).
15. Maurice, V., Strehblow, H. & Marcus, P. In situ STM study of the initial stages of oxidation of Cu (111) in aqueous solution. *Surf. Sci.* **458**, 185–194 (2000).
16. Kosmala, T., Blanco, M., Granozzi, G. & Wandelt, K. Porphyrin bi-layer formation induced by a surface confined reduction on an iodine-modified Au(100) electrode surface. *Electrochim. Acta* **360**, 137026 (2020).
17. Facchin, A. A., Kosmala, T., Gennaro, A. & Durante, C. Electrochemical Scanning Tunnelling Microscopy investigations of FeN4 based macrocyclic molecules adsorbed on Au(111) and their implications in Oxygen Reduction Reaction. *ChemElectroChem* (2020) doi:10.1002/celc.202000137.
18. Pfisterer, J. H. K., Liang, Y., Schneider, O. & Bandarenka, A. S. Direct instrumental identification of catalytically active surface sites. *Nature* **549**, 74–77 (2017).
19. Liang, Y., Mclaughlin, D., Csoklich, C., Schneider, O. & Bandarenka, A. S. The nature of active centers catalyzing oxygen electro-reduction at platinum surfaces in alkaline media. *Energy Environ. Sci.* **12**, 351–357 (2019).
20. Dedkov, Y. S., Fonin, M., Rüdiger, U. & Laubschat, C. Graphene-protected iron layer on Ni(111). *Appl. Phys. Lett.* **93**, 85–88 (2008).
21. Sutter, P., Sadkowski, J. T. & Sutter, E. Graphene on Pt(111): Growth and substrate interaction. *Phys. Rev. B* **80**, 245411 (2009).
22. Cattelan, M. *et al.* The dynamics of Fe intercalation on pure and nitrogen doped graphene grown on Pt(111) probed by CO adsorption. *Surf. Sci.* **634**, 49–56 (2015).
23. Dahal, A. & Batzill, M. Growth from behind: Intercalation-growth of two-dimensional FeO moiré structure underneath of metal-supported graphene. *Sci. Rep.* **5**, 1–9 (2015).
24. Cattelan, M. *et al.* The nature of the Fe-graphene interface at the nanometer level. *Nanoscale* **7**, 2450–2460 (2015).
25. Hamada, I. & Otani, M. Comparative van der Waals density-functional study of graphene on metal surfaces. *Phys. Rev. B - Condens. Matter Mater. Phys.* **82**, 1–4 (2010).
26. Fu, Y., Rudnev, A. V., Wiberg, G. K. H. & Arenz, M. Single Graphene Layer on Pt(111) Creates Confined Electrochemical Environment via Selective Ion Transport. *Angew. Chemie - Int. Ed.* **56**, 12883–12887 (2017).
27. Miao, M., Nardelli, M. B., Wang, Q. & Liu, Y. First principles study of the permeability of graphene to hydrogen atoms. *Phys. Chem. Chem. Phys.* **15**, 16132–16137 (2013).
28. Hu, K. *et al.* Catalytic activity of graphene-covered non-noble metals governed by proton penetration in electrochemical hydrogen evolution reaction. *Nat. Commun.* **12**, 1–3 (2021).
29. Reda, M., Hansen, H. A. & Vegge, T. DFT Study of the Oxygen Reduction Reaction on Carbon-Coated Iron and Iron Carbide. *ACS Catal.* **8**, 10521–10529 (2018).
30. Zhou, Y. *et al.* Enhancing the Hydrogen Activation Reactivity of Nonprecious Metal Substrates via Confined Catalysis Underneath Graphene. *Nano Lett.* **16**, 6058–6063 (2016).
31. Nørskov, J. K. *et al.* Trends in the Exchange Current for Hydrogen Evolution. *J. Electrochem. Soc.* **152**, J23 (2005).
32. Markovic, N. M., Grgur, B. N. & Ross, P. N. Temperature-Dependent Hydrogen

Electrochemistry on Platinum Low-Index Single-Crystal Surfaces in Acid Solutions. *J. Phys. Chem. B* **5647**, 5405–5413 (1997).
33. Hu, S. *et al.* Proton transport through one-atom-thick crystals. *Nature* **516**, 227–230 (2014).
34. Achtyl, J. L. *et al.* Aqueous proton transfer across single-layer graphene. *Nat. Commun.* **6**, 1–7 (2015).
35. Xu, J. *et al.* Transparent proton transport through a two-dimensional nanomesh material. *Nat. Commun.* **10**, 1–8 (2019).
36. Amokrane, N., Gabrielli, C., Ostermann, E. & Perrot, H. Investigation of hydrogen adsorption-absorption on iron by EIS. *Electrochim. Acta* **53**, 700–709 (2007).
37. Repetto, D. *et al.* Structure and magnetism of atomically thin Fe layers on flat and vicinal Pt surfaces. *Phys. Rev. B - Condens. Matter Mater. Phys.* **74**, 1–8 (2006).
38. Tavakkoli, M. *et al.* Single-Shell Carbon-Encapsulated Iron Nanoparticles: Synthesis and High Electrocatalytic Activity for Hydrogen Evolution Reaction. *Angew. Chemie - Int. Ed.* **54**, 4535–4538 (2015).
39. Carnevali, V. *et al.* Doping of epitaxial graphene by direct incorporation of nickel adatoms. *Nanoscale* **11**, 10358–10364 (2019).
40. Cilpa-karhu, G., Pakkanen, O. J. & Laasonen, K. Hydrogen Evolution Reaction on the Single-Shell Carbon- Encapsulated Iron Nanoparticle : A Density Functional Theory Insight. *J. Phys. Chem. C* **123**, 13569–13577 (2019).
41. Schmid, M. *et al.* On-Surface Synthesis and Characterization of an Iron Corrole. *J. Phys. Chem. C* **122**, 10392–10399 (2018).
42. Tabassum, H. *et al.* Recent advances in confining metal-based nanoparticles into carbon nanotubes for electrochemical energy conversion and storage devices. *Energy Environ. Sci.* **12**, 2924–2956 (2019).
43. Calvillo, L. *et al.* Electrochemical Behavior of TiOxCy as Catalyst Support for Direct Ethanol Fuel Cells at Intermediate Temperature: From Planar Systems to Powders. *ACS Appl. Mater. Interfaces* **8**, 716–725 (2016).
44. Fadley, C. S. Angle-resolved x-ray photoelectron spectroscopy. *Progr. Surf. Sci.* **16**, 275–388 (1984).
45. Http://www.kolibrik.net/science/kolxpd/. http://www.kolibrik.net/science/kolxpd/.
46. Wilms, M., Kruft, M., Bermes, G. & Wandelt, K. A new and sophisticated electrochemical scanning tunneling microscope design for the investigation of potentiodynamic processes. *Rev. Sci. Instrum.* **70**, 3641 (1999).
47. Horcas, I. *et al.* WSXM : A software for scanning probe microscopy and a tool for nanotechnology. *Rev. Sci. Instrum.* **78**, 1–8 (2007).
48. Giannozzi, P. *et al.* QUANTUM ESPRESSO: A modular and open-source software project for quantum simulations of materials. *J. Phys. Condens. Matter* **21**, (2009).
49. Tersoff, J. & Hamann, D. R. Theory of the scanning tunneling microscope. *Phys. Rev. B* **31**, 805–813 (1985).
50. Kaack, M. & Fick, D. Determination of the work functions of Pt(111) and Ir(111) beyond 1100 K surface temperature. *Surf. Sci.* **342**, 111–118 (1995).
51. Monkhorst, H. J. & Pack, J. D. Special Points for Brillouin-Zone Integrations. *Phys. Rev. B* **13**, 5188–5192 (1976).
52. Thonhauser, T. *et al.* Spin Signature of Nonlocal Correlation Binding in Metal-Organic Frameworks. *Phys. Rev. Lett.* **115**, 1–6 (2015).

53. Thonhauser, T. *et al.* Van der Waals density functional: Self-consistent potential and the nature of the van der Waals bond. *Phys. Rev. B - Condens. Matter Mater. Phys.* **76**, 1–11 (2007).
54. Berland, K. *et al.* van der Waals forces in density functional theory: a review of the vdW-DF method. *Reports Prog. Phys.* **78**, (2015).
55. Langreth, D. C. *et al.* A density functional for sparse matter. *J. Phys. Condens. Matter* **21**, (2009).
56. Nørskov, J. K. *et al.* Origin of the overpotential for oxygen reduction at a fuel-cell cathode. *J. Phys. Chem. B* **108**, 17886–17892 (2004).
57. García-Gil, S., García, A. & Ordejón, P. Calculation of core level shifts within DFT using pseudopotentials and localized basis sets. *Eur. Phys. J. B* **85**, (2012).
58. Baby, A. *et al.* Lattice Mismatch Drives Spatial Modulation of Corannulene Tilt on Ag(111). *J. Phys. Chem. C* **122**, 10365–10376 (2018).
59. Baby, A., Lin, H., Brivio, G. P., Floreano, L. & Fratesi, G. Core-level spectra and molecular deformation in adsorption: V-shaped pentacene on Al(001). *Beilstein J. Nanotechnol.* **6**, 2242–2251 (2015).
60. Kokalj, A. XCrySDen-a new program for displaying crystalline structures and electron densities. *J. Mol. Graph. Model.* **17**, 176–179 (1999).

Acknowledgements

The computations were run on the supercomputer MARCONI at CINECA, Bologna, Italy.
This work has been partially supported by the project "MADAM - Metal Activated 2D cArbon-based platforMs" funded by the Italian MIUR (PRIN 2017) - grant 2017NYPHN8, MIUR (PRIN 2015: SMARTNESS, 2015K7FZLH; PRIN2017: Multi-e, 20179337R7) and the MAECI Italy–China Bilateral Project (GINSENG, PGR00953). Cariparo foundation is acknowledged for funding (project Synergy, Progetti di Eccellenza 2018). The University of Wrocław is also acknowledged for the financial support 1010/S/IFD.-We acknowledge the technical support for the EC-STM instrumentation by Alessandro Facchin.

Author contributions

Competing interests

The authors declare no competing interests

Additional information

Supplementary information

784
785